Thermal Flow Sensors for Intravascular Shear Stress Analysis

by

Rui Tang

A Thesis Presented in Partial Fulfillment
of the Requirements for the Degree
Master of Science

Approved July 2011 by the
Graduate Supervisory Committee:

Hongyu Yu, Chair
Hanqing Jiang
George Pan

ARIZONA STATE UNIVERSITY

December 2011

ABSTRACT

This thesis investigated two different thermal flow sensors for intravascular shear stress analysis. They were based on heat transfer principle, which heat convection from the resistively heated element to the flowing fluid was measured as a function of the changes in voltage. For both sensors, the resistively heated elements were made of Ti/Pt strips with the thickness 0.12 μm and 0.02 μm. The resistance of the sensing element was measured at approximately 1.6-1.7 kΩ. A linear relation between the resistance and temperature was established over the temperature ranging from 22 ˚C to 80 ˚C and the temperature coefficient of resistance (TCR) was at approximately 0.12 %/˚C.

The first thermal flow sensor was one-dimensional (1-D) flexible shear stress sensor. The structure was sensing element sandwiched by a biocompatible polymer "poly-para-xylylene", also known as Parylene, which provided both insulation of electrodes and flexibility of the sensors. A constant-temperature (CT) circuit was designed as the read out circuit based on 0.6 μm CMOS (Complementary Metal–Oxide–Semiconductor) process.

The 1-D shear stress sensor suffered from a large measurement error. Because when the sensor was inserted into blood vessels, it was impossible to mount the sensor to the wall as calibrated in micro fluidic channels. According to the previous simulation work, the shear stress was varying and the sensor itself changed the shear stress distribution.

We proposed a three-dimensional (3-D) thermal flow sensor, with three-axis of sensing elements integrated in one sensor. It was in the similar shape as a

hexagonal prism with diagonal of 1000 μm. On the top of the sensor, there were five bond pads for external wires over 500 μm thick silicon substrate. In each nonadjacent side surface, there was a bended Parylene branch with one sensing element.

Based on the unique 3-D structure, the sensor was able to obtain data along three axes. With computational fluid dynamics (CFD) model, it is possible to locate the sensor in the blood vessels and give us a better understanding of shear stress distribution in the presence of time-varying component of blood flow and realize more accurate assessment of intravascular convective heat transfer.

DEDICATION

To My Mother and Father

ACKNOWLEDGMENTS

I would like to express my special appreciation to my academic advisor, Dr. Hongyu Yu for providing me a chance to work on such an innovative project, which paves the way to build my thesis. It is such a great privilege to work with him. I am also thankful to my advisory committee members, Dr. Hanqing Jiang, Dr. George Pan for taking interest in my work and giving valuable advice to me.

I am grateful to members of our group: Dr. Xiaotun Qiu, Dr. Yong, Jon Oiler, Hai Huang, Teng Ma, and Bryce Carande. Their help and advice are the main resources for me to overcome any difficulties. From them, I am always inspired, motivated, and encouraged. I enjoy not only working together in the same group, but also the friendship in the daily life.

I am also grateful to my parents, who give me full support on whatever decision I make throughout my life and do their best to provide me a good education at home and an opportunity to study abroad.

Finally, I want to thank all my friends at Arizona State University, Huazhong University of Science and Technology, for their moral and technical support, without which I would not have succeeded in finishing my study.

TABLE OF CONTENTS

Page

LIST OF TABLES

Table Page

LIST OF FIGURES

Figure Page

Figure Page

Figure Page

Figure Page

Chapter 1

INTRODUCTION

Flow sensors, often used in measurements of flow speed and direction, flow separation detection, pressure, and wall-shear stress, are extremely important for making a variety of different fluid dynamic measurements ranged from industry (e.g. in process control for dosing reagents and combustibles, in cooling and purification plants) to domestic monitoring of potable water. Such wide and particular application fields brought to a consequent development of various typologies of flow sensors which differ each other for the operating measurement principle.

However, they are typically expensive and cumbersome; sometime induce huge perturbations in the measured environment. With the recent developments in silicon micromachining technology, both the sensing elements and the conditioning electronics can be integrated in microelectromechanical systems (MEMS) devices featuring a drastic reduction in cost, area, and power, leading to harder disturbances rejection due to the thigh interconnection reduction. The scaling down of the sensor size also allows faster response to be obtained and guarantees a higher reliability, reducing movable structures.

There are several types of measurement methodologies for flow detection based on different physical principles according to the particular environment. Some sensors perform flow detection through a pressure variation in the measuring line obtained with porous sections or different section size in the line. Other sensors exploit area variation, fluid dynamic turbulences, or mechanical

turbine wheel (Elwenspoek 1999). All above mentioned sensors perform an "intrusive" measurement; this kind of method can also be called direct measurement. Since they induce a perturbation in the flow under test due to the considerable interaction between the sensor and the fluid itself (e.g. a pressure loss), these devices usually require a consistent effort in setting up the sensing equipment on the line under test. Another disadvantage of mechanical flow sensors lies in the dependence of the force, pressure difference and fluid density. The density of most fluids depends on the temperature. Therefore, a temperature compensation is a compelling necessity (Nguyen 1997).

Another class of "non-intrusive" sensors performs the measurement without affecting the flow under test, basing their interaction on energy transfer, (thermal, ultrasonic or electro-magnetic) (Van Oudheusden 1988, Rasmussen and Zaghloul 1998 and Ashauer et al. 1998). These sensors avoid moving structures thus resulting more compact and robust and easier to manufacture, satisfying the requirements for micromachining tooling. However, electromagnetic sensors, in order to achieve good sensitivity, require a sufficient magnetic induction which is not easy to be provided in MEMS fabrication process, while technological problems arises with devices for emitting and receiving ultrasounds, especially when they are in liquid flow. Thus, thermal sensors are considered to be promising candidates for MEMS integration due to their relatively small thickness, good sensitivity and simple structures. This thesis will only cover the thermal sensors. Typically, this is performed by injecting heat into the flow and using convection principles to determine properties of the flow. The use of heat to

determine flow dynamics as well as fabrication processes that permit relatively small and flat surfaces, results in very little flow perturbation and allows more accurate measurements. The elimination of moving parts make these devices robust and thermal measurements also offer the possibility of measuring time-varying flows.

Thermal flow sensors generally operate on one of three operating principles (Elwenspoek 1999). The first principle is called calorimetry. It is defined that thermal mass flow sensors measure the asymmetry of temperature profile around the heater which is modulated by the fluid flow (Nguyen 1997), shown in Fig. 1.1.

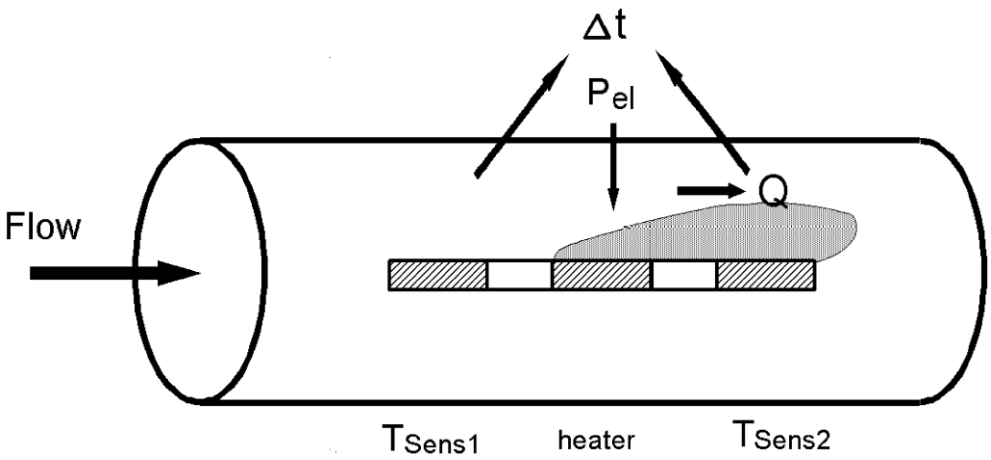

Figure 1.1 Calorimetry measurement (Ashauser and Glosch 1999).

Here the fluid is heated up by a central resistor. Temperature sensors arranged symmetrically upstream and downstream of the flow are used to determine the temperature of the fluid (and thus speed) and the direction of the flow. A central resistor (heater) injects heat into the fluid, which increases the water temperature in a small boundary layer. The water is carried downstream where it flows over a downstream temperature sensor (often called a thermistor).

The downstream thermistor, originally at ambient temperature, will now be convectively heated from the higher temperature water within the small boundary layer (Ashauser and Glosch 1999). The upstream (opposite of flow direction) thermistor measures the temperature of the flow via its temperature-dependent resistance. The thermistors are located very close to the central heater. Measuring flow speed via the heat exchange between the flow and the thermistors is less accurate than anemometry for high flow speeds (Nguyen 1997). Keeping the thermistors near the central heater can improve measurement sensitivity, however, the close positioning to the heat source can create additional measurement errors due to heat more readily passing conductively from the heater to the thermistors through the substrate.

The second thermal principle is thermal time of flight. It is defined that thermal mass flow sensors measure the passage of time of a heat pulse over a known distance (Nguyen 1997), shown in Fig. 1.2.

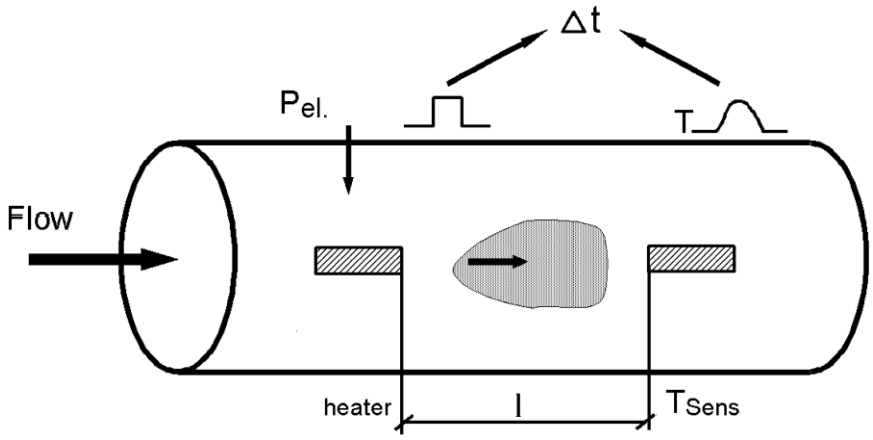

Figure 1.2 Thermal time-of-flight measurement (Ashauser and Glosch 1999).

In this scenario a pulse of heat is delivered to the flow at a central location. When the pulse is delivered a clock timer begins. The heat is carried downstream

where it flows over a temperature sensor which is convectively heated. When the temperature sensor (such as a thermistor) output registers a maximum in temperature, the time is recorded. By fabricating the thermistors at a known distance from the location of the heat pulse, the velocity can be determined by taking this distance and dividing by the amount of time passed before the temperature maximum is recorded. By placing temperature sensors symmetrically around the heating source, the direction of the flow can be determined as well. Because the heat will diffuse in the water, more accurate results are obtained by setting the temperature sensors extremely close to the heating element. However, as noted before, conduction through the substrate becomes an issue and limits how close the temperature sensors can get to the heater.

The third principle is anemometry. It is defined that thermal mass flow sensors measure the effect of the flowing fluid on a hot body (increase of heating power with constant heater temperature, decrease of heater temperature with constant heating power) (Nguyen 1997), shown in Fig. 1.3.

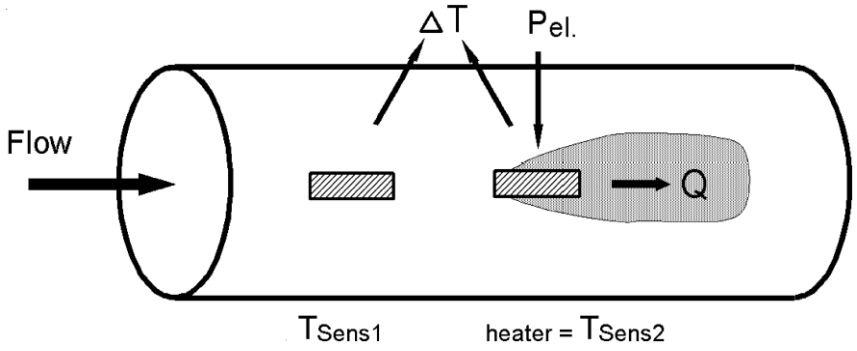

Figure 1.3 Anemometer measurement (Ashauser and Glosch 1999).

An anemometer involves exposing a heated resistor (heater) to a moving fluid. When the heater's temperature is higher than the surrounding fluid, heat

energy is transferred to the moving fluid via convection, increasing the water temperature within a small boundary layer. The power input to this heater is used to determine the speed of the flow via

$$P_{IN} = P_{OUT} \Rightarrow i^2 R = hA\Delta T \qquad \text{(Eq. 1.1)}$$

where on the left-hand side of the above equation, i represents the input current to the heater and R is the heater resistance. The right-hand side of the equation represents the heat loss of the anemometer system due to convection. Here we assume that radiative heat loss is negligible as is the heat loss through conduction. Ignoring radiative heat loss is an accurate assumption because of the extremely small surface area of the anemometer and the small difference in operating temperature between the heater and flow.

The convective heat equation is composed of three terms. The first term, h, represents the convective heat transfer coefficient. The second term, A, represents the area of the surface over which the heat transfer occurs, and the last term, ΔT, represents the difference in temperature between the liquid flow and the heater surface. The convective heat transfer coefficient carries the flow speed information:

$$h = a + bv^c \qquad \text{(Eq. 1.2)}$$

where a, b, and c are empirically determined constants that are characterized through the calibration of the sensor and v represents the speed of the flow which is the unknown variable in the heat transfer equation. From (Eq. 1.1) and (Eq. 1.2) we obtain:

$$v = \left(\frac{i^2 R}{bA\Delta T} - \frac{a}{b} \right)^{1/c} \quad \text{(Eq. 1.3)}$$

which represents the final form of the convective heat transfer equation. The anemometer principle provides a sensitive and accurate method for measuring the flow velocity because the amount of heat convectively delivered to the flow is measured directly by the power input to the resistor. However, an anemometer alone cannot provide any information on flow direction.

Fluid shear stress (τ) is another important property of the flow which is emphasized in this thesis. It is a frictional force per unit area that is tangential to the surface of the channel. For a Newtonian fluid at steady state, shear stress τ is defined as (Yu et al. 2008)

$$\tau = \eta \frac{dv}{dy} \quad \text{(Eq. 1.4)}$$

where η represents viscosity and dv/dy is the velocity gradient along the y-axis which is perpendicular to the wall surface (Fig. 1.4). Therefore, based on the linear relation between flow shear stress and velocity gradient along y-axis, the dependence of wall shear stress on the heat transfer and thus voltage can be obtained by combining Eq. 1.3 and Eq. 1.4, which follows an experienced equation (Haritonidis 1989):

$$P = (T - T_0)(A + B\tau^{1/3}) \quad \text{(Eq. 1.5)}$$

where T_0 is the temperature of the ambient flow and T is the sensor temperature, P is the heating power for the sensor to compensate for the heat convection and A and B are calibration constants.

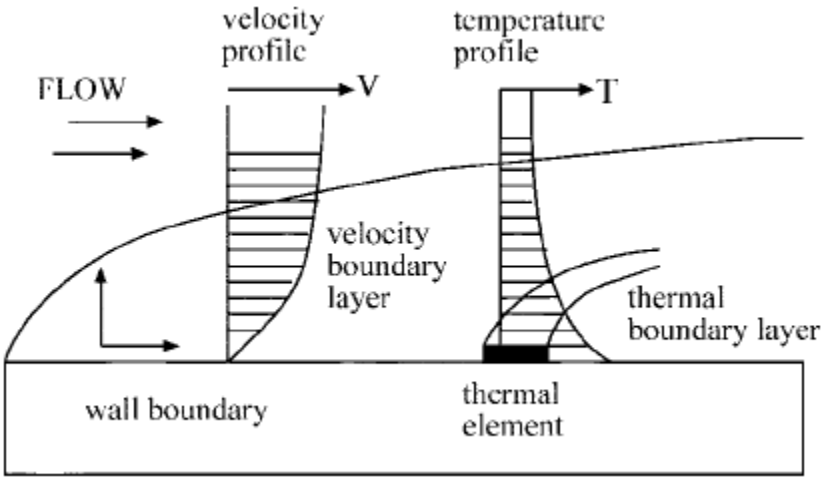

Figure 1.4 Principle of thermal shear stress sensor. The heat loss from a heated resistive element to the fluid flow is dependent on the wall shear stress and hence the velocity gradient along y-axis.

The anemometer principle provides a sensitive and accurate method (Table 1.1) for measuring the flow velocity and shear stress because the amount of heat convectively delivered to the flow is measured directly by the power input to the resistor. Anemometer can be operated by one of two types of control and readout modes: constant-current (CC) and constant-temperature (CT) modes. Fig. 1.5 shows a basic constant-current-type circuit for heating an anemometer (hot-wire probe).

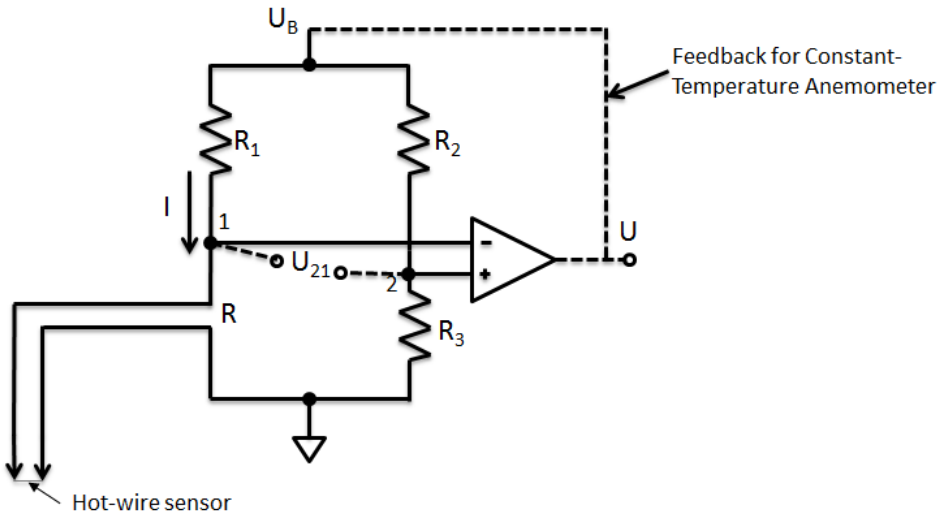

Figure 1.5 Basic control circuit of a hot-wire anemometer.

Assuming a linear relation between temperature and resistance, the resistance R of the sensor can be represented as

$$R=R_r[1+\alpha(T_m - T_r)] \qquad \text{(Eq. 1.6)}$$

where R_r is resistance at reference temperature T_r, T_m is the sensor operating temperature, and α is temperature coefficient of the resistance. In Fig. 1.5, if the resistance of R_1 is much larger in comparison with that of the sensor (R), then the current I is nearly constant, and any increase of flow velocity from the surrounding fluid will cause the sensor to cool. Because of the temperature coefficient of resistance α, this cooling will cause a decrease in R, an increase in U_{21}, and an increase in amplifier output U.

Table 1.1 Comparison of various flow sensors

Type	Transducing principle	Comparison
Direct flow measurement (Non-thermal flow sensor)	Mechanical deformation (cantilever bending)	Larger surface area, inducing perturbations to flow, temperature compensation problem.
Calorimetry (thermal flow sensor)	A resistor Temperature sensors needed (thermoresistive, thermopile)	Less accurate in high flow speeds measurement. Thermopile is more accurate, but space consuming (hundreds square microns).
Time of flight (thermal flow sensor)	A resistor Temperature sensors needed (thermoresistive, thermopile)	Temperature sensors extremely close to the heating element, conduction through the substrate becomes an issue. Narrow full flow scale.
Anemometry (thermal flow sensor)	Resistive materials as heaters (thermoresistive)	Single sensor incapable of measuring flow direction. Substrate conduction issue.

Adding a feedback line (shown in Fig. 1.5) converts a CC circuit to a CT system. The feedback from the output of the amplifier to the top of the resistor bridge acts to maintain the resistance of the sensor and hence the average temperature essentially constant. Fig. 1.6 shows a typical measurement results for anemometer operated in CC and CT modes. CT mode normally has a higher sensitivity than that of the CC mode.

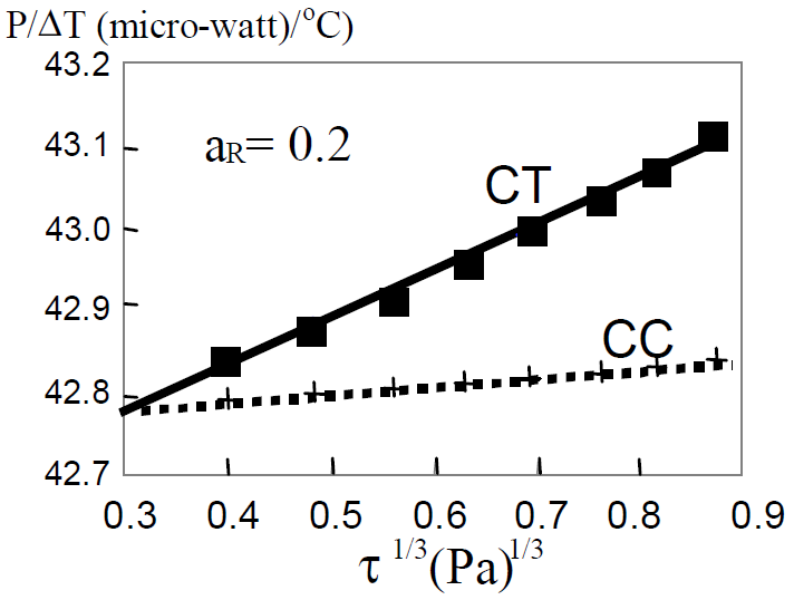

Figure 1.6 Typical sensor characteristic of hot-wire type in CT mode and CC mode (Liu et al. 1999).

The first thermal flow sensor based on silicon technology was published by van Putten and Middelhoek of the University of Technology, Delft in 1974. The sensor was developed to an integrated silicon double bridge anemometer (Van Putten 1983).

After that, different materials were applied to work as sensing element. Toyota Central Research and Development Laboratories developed another thermoresistive silicon flow sensor in 1985 (Tabata et al. 1985) based on the conventional hot-film anemometry principle (Fig. 1.7). The sensor chip has two platinum thin-film resistors which are used as a heating element and a fluid temperature sensing element. The resistors are located in the center of the oxidized porous silicon diaphragm and the rim of the chip, respectively.

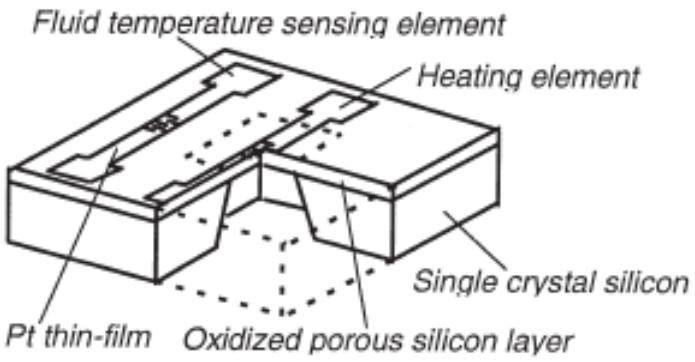

Figure 1.7 Structure of the sensor chip of Toyota Central Research and Development Laboratories (Tabata et al. 1985).

As the development of CMOS technology and the compatibility of the surface micromachining and CMOS process, thermal flow sensors with heater and temperature sensing element made by CMOS field effect transistors (FETs) and integrated with CMOS control chip were developed by G. Stemme (1988) (Fig. 1.8).

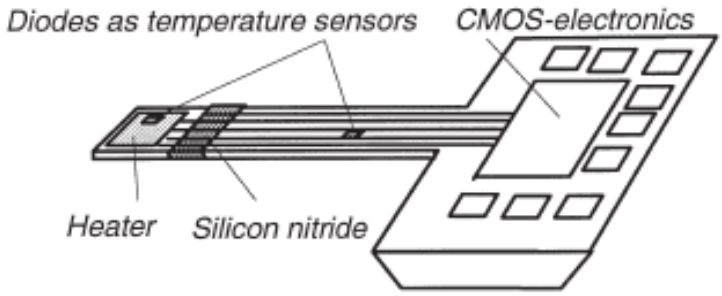

Figure 1.8 A schematic drawing of the thermal flow sensor integrated with the CMOS control circuit. (G. Stemme 1988).

Above thermal micro flow sensors were mainly designed to detect velocity and direction of gas flow. After 1990s, thermal flow sensors focused on wall shear stress was developed, because of the importance of wall shear stress in fluid mechanics, aerodynamics studies and biomedical applications. Liu et al. designed

a micromachined flow shear stress sensor based on thermal transfer principles. In the same time, with the introducing of polymer package, MEMS flow sensors for underwater application was intensively researched on (Fan et al. 2004 and Melani et al. 2008). Recently, flexible thermal flow sensors or sensors fabricated on flexible substrates were drawing more and more attention due to their promising future in biomedical applications using polymer, especially biocompatible material Parylene.

The thesis is arranged in the following manners. In Chapter 1, an introduction to various flow measurement mechanisms was given. And a brief review of MEMS thermal flow sensor including working principle, structure design and read-out circuit was emphasized. In Chapter 2, a 1-D flexible thermal flow sensor for intravascular shear stress analysis was investigated and constant-temperature read-out circuit design was discussed. Chapter 3 presented a 3-D (3-axis of sensing elements) thermal flow sensor for detecting changes in intravascular convective heat transfer. At last in Chapter 4, conclusions and future work of this thesis were presented.

Chapter 2

FLEXIBLE THERMAL FLOW SENSORS FOR INTRAVASCULAR SHEAR STRESS ANALYSIS

Coronary heart disease is still the leading vital disease worldwide according to the World Health Organization. Hemodynamic forces, specifically fluid shear stress, play an important role in the development of coronary artery disease (Nerem et al. 1998, Topper et al. 1996, Ku 1997, Davies et al. 1984, Soulis et al. 2006, Frauenfelder et al. 2007) (shear stress and hemodynamic force). The development of MEMS thermal flow sensors provides an entry point for assessment of small-scaled hemodynamics with high spatial and temporal variations (Rouhanizadeh et al. 2006) otherwise difficult with computed tomography, magnetic resonance imaging, ultrasound, and laser Doppler velocimetry.

MEMS shear stress sensors have been developed for aerodynamics and fluid mechanics (Lin et al. 2004, Liu et al. 1994). A flexible shear-stress sensor skin containing a 1-D array of 36 shear stress sensors has been designed to acquire shear stress measurement on the nonplanar surfaces (Xu et al. 2003). Previously, MEMS shear stress sensor with backside wire bonding to address microscale hemodynamics with high temporal and spatial resolutions was fabricated (Rouhanizadeh et al. 2006). However, to assess shear stress in the complicated arterial geometry in the presence of time-varying component of blood flow, we developed a new generation of polymer based sensors that are flexible, biocompatible, and deployable into the arterial system.

2.1 Wall shear stress measurement

As briefly mentioned in Chapter 1, fluid shear stress (τ) is of great importance property of the flow. It is a frictional force per unit area that is tangential to the surface of the channel. For a Newtonian fluid at steady state, shear stress τ is defined as (Yu et al. 2008)

$$\tau = \eta \left. \frac{dv}{dy} \right|_{y=0} \qquad \text{(Eq. 2.1)}$$

where η represents viscosity and dv/dy is the velocity gradient along the y-axis which is perpendicular to the wall surface. Two main methods for shear stress measurement have been developed. The first one is to build a floating sensing element (Schmidt et al. 1988). The advantage of such a design is direct measurements rather than indirect correlations between shear stress and other parameters, such as heat transfer. However, the sensing elements of floating sensors are usually difficult to fabricate, some structures are fragile. Their operation requires additional mechanical devices to amplify signal transduction in response to minute movements. In addition, extra mechanical structures usually cause perturbation to flow itself. Due to above problems, the second one, which is thermal anemometry, is more widely used. The advantages of this technique are simplicity in fabrication, absence of moving elements, and good sensitivity. Thus, this method provides a basis to develop micro intravascular sensors on a single silicon wafer for high throughput production.

The operation principle is based on convective cooling of a heated sensing element as fluid flows over its surface. The heat transfer from the heated surface

to the fluid depends on the flow characteristics in the viscous region of the boundary layer (Liu et al. 1994) (Fig. 2.1).

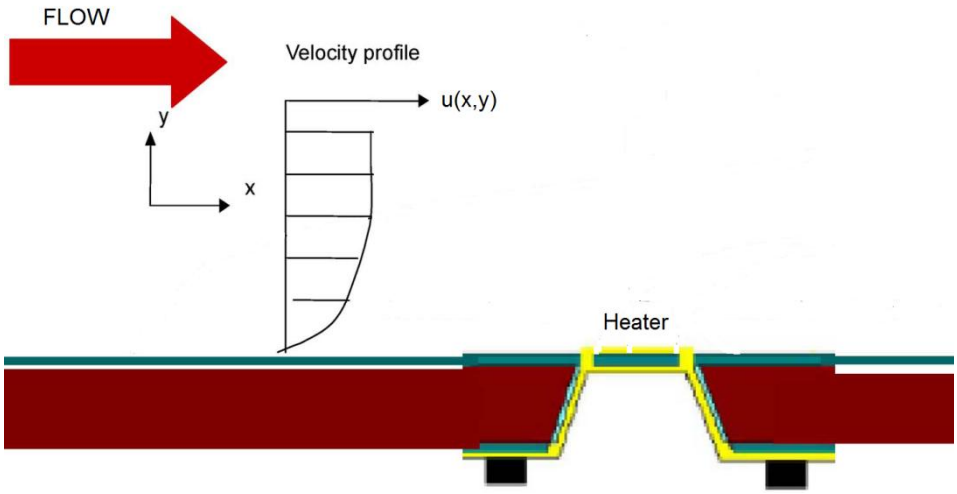

Figure 2.1 A thermal boundary develops beneath the flow velocity boundary layer (Liu et al. 1994).

This concept was simulated by FEA analysis tool ANSYS 11.0. The simulation was based on a simple and ideal model for demonstration. The temperature distribution profile of a water channel was simulated. In the middle of the channel, there was a plate (about 1/3 of the total length) heated to 47 ˚C, 10 ˚C above ambient temperature (37 ˚C) (Fig. 2.2). The whole channel was 3mm in length and 1mm in width. For the simulation, only natural convection energy losses had been taken into account since the irradiative and conduction energy losses are very small due to the small area of the heated plate.

Different velocity of water flow is introduced (0.2m/s and 0.5m/s). Different temperature profiles are presented in Fig. 2.3. The heat transfer water flow passes by the heated sensing element, the faster the velocity is, the more heat it will take away, in this way, making the high temperature thinner.

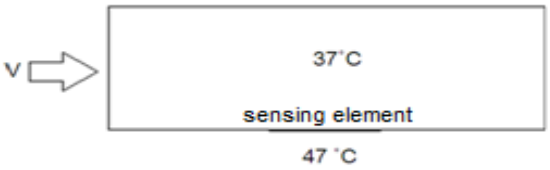

Figure 2.2 ANSYS simulation environment

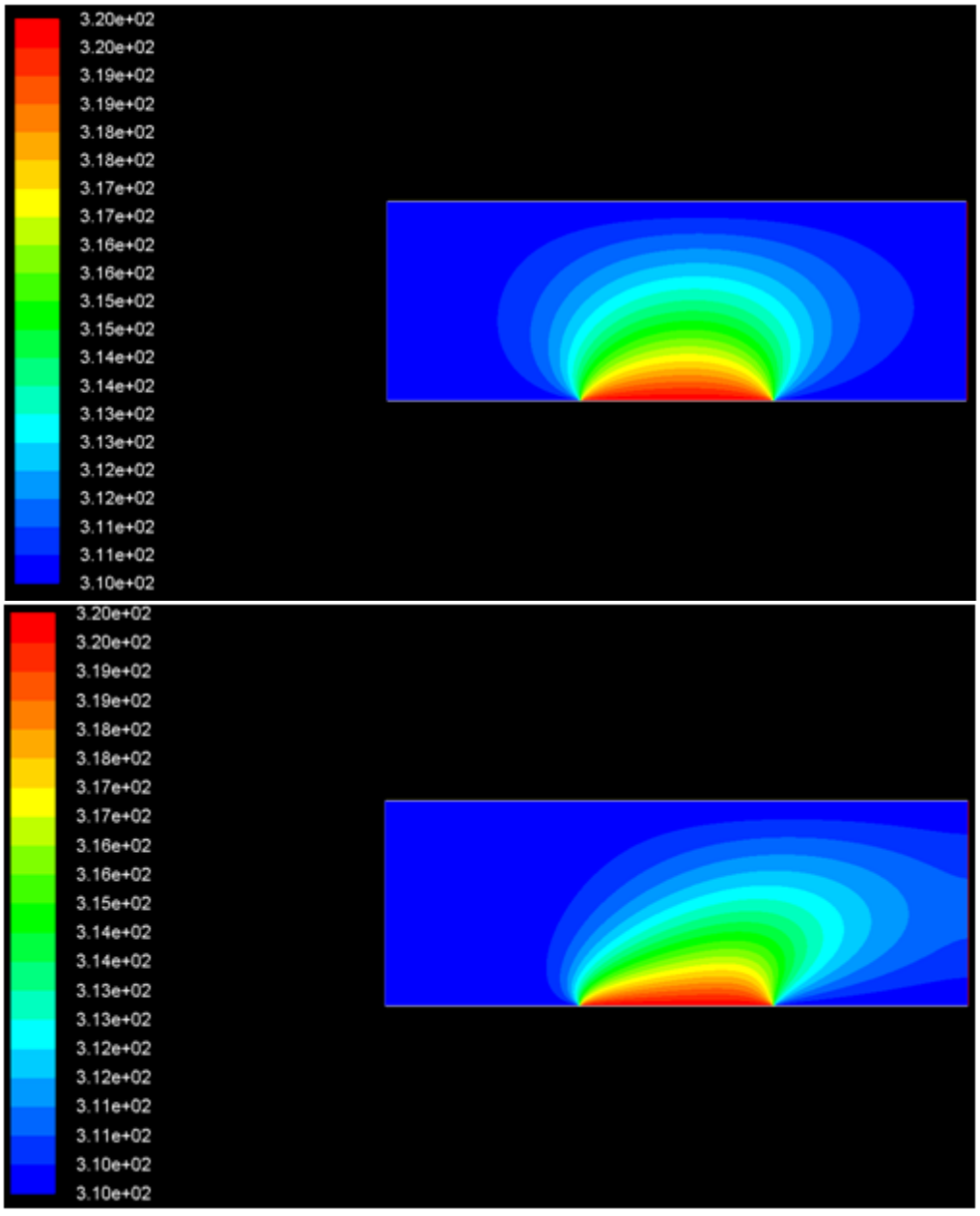

Figure 2.3 Temperature distribution of the water channel with different water velocities

2.2 Design and fabrication of 1-D flexible shear stress sensors

Titanium (Ti) and platinum (Pt) layers embedded in the flexible polymer were used as the sensing elements. Based on heat transfer principle, heat convection from the resistively heated element to the flowing fluid is measured as a function of the changes in voltage, from which shear stress can be inferred (Liu et al. 1994). The sensor was fabricated by surface micromachining technique utilizing Parylene C as electrical insulation layer.

The polymer-embedded sensor enables conformability to the geometry of arterial bifurcations and curvatures while retaining its mechanical strength and operational function. The resistance of the sensing element was measured at approximately 1.6-1.7 kΩ and the temperature coefficient of resistance (TCR) was at approximately 0.12 %/˚C, shown in Fig. 2.4.

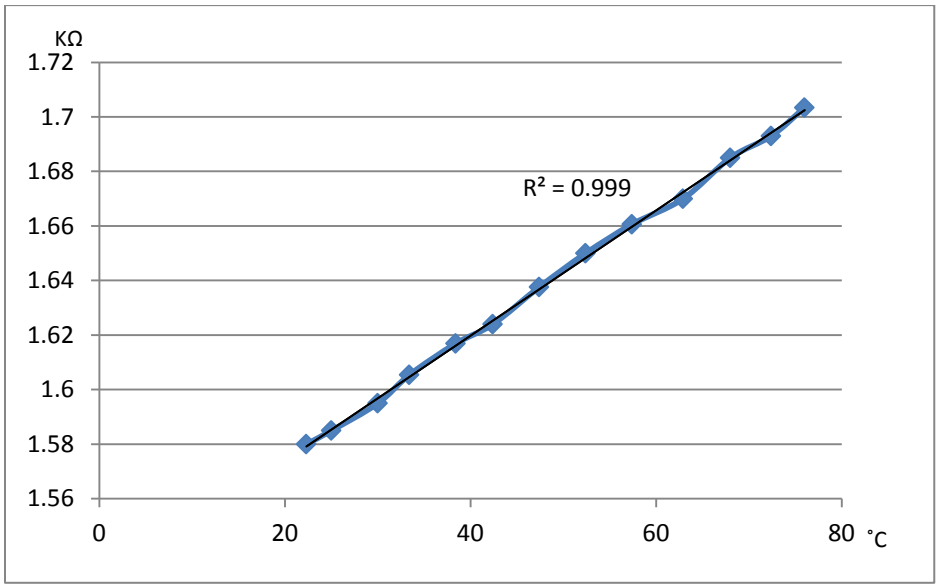

Figure 2.4 Plot of sensing element (Ti/Pt) resistance versus temperature. A linear relation was established over the temperature ranging from 22 ˚C to 80 ˚C. The TCR was approximately 0.12 %/˚C.

For the package, the sensing element was connected to a flexible electrical coaxial wire (40AWG wire from Tycoelectronics) that transmitted the changes in resistance to the external circuitry. Due to the small size of the sensor, the bonding process is implemented on the probestation under microscope (Fig. 2.5).

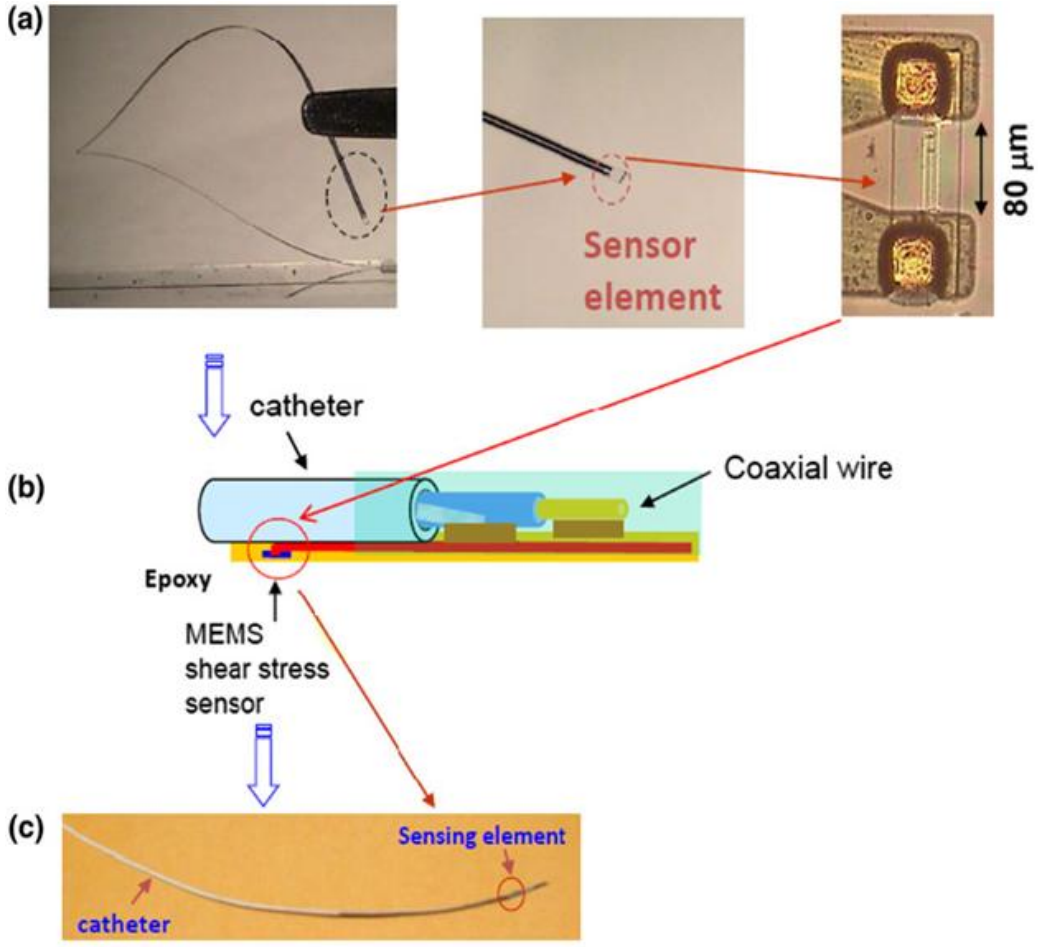

Figure 2.5 The flexible shear stress sensors. (a) The sensor was flexible. The dotted circle at the terminal end of sensor was magnified to reveal the polymer-coated sensing element. (b) The schematic diagram detailed the packaging of the polymer sensor to the coaxial wire. The sensor was connected to the electrical coaxial wire with conductive epoxy and covered with biocompatible epoxy. The distance between the sensing element and the tip of the catheter was 4 cm. (c) Illustration revealed a packaged sensor to the coaxial wire.

The sensing element was fabricated using surface micromachining with biocompatible materials including Ti, Pt and Parylene C. Parylene is the tradename for a variety of chemical vapor deposited poly(p-xylylene) polymers used as moisture and dielectric barriers. Among them, Parylene C is the most popular due to its combination of barrier properties, cost, and other processing advantages. The fabrication process is as the following: 1) dry thermal growth of 0.3 μm SiO_2 (1080 ˚C for approximately 4 hours according to Deal and Grove (D-G) thermal oxidation model), then deposit 1 μm sacrificial silicon layer (polysilicon) using electron-beam (e-beam) evaporator. This layer will be etched completely during the sensor releasing; 2) dry thermal growth of approximately 0.2 μm SiO_2 and use BOE (Buffered Oxide Etchant) to pattern SiO_2 layer. 3) deposit Ti/Pt layers with thickness of 0.12 μm/0.02 μm for the sensing element with e-beam evaporator, and pattern these layers using lift-off (AZ5214 negative photoresist) to form a 2-3 μm wide metal traces; 4) deposit 9 μm Parylene C with Parylene vacuum coating system and pattern Parylene C layer using photolithography and oxygen plasma. Because the etching rate between Parylene C and photoresist is very close, approximately 7:8, the Parylene C is etched even faster, more than 10 μm thick photoresist is needed; 5) deposition and patterning of a metal layer of Cr/Au for electrode leads (0.02 μm/0.6 μm) with e-beam evaporator; 6) deposition of another thick layer of Parylene C (12 μm) to form the device structure, then pattern it using AZ4620 photoresist up to 20 μm as mask; 7) etching the underneath silicon sacrificial layer with XeF_2 dry etching system leading to the final device included in Fig. 2.6. The resulting sensor bodies were 4

cm in length, 320 μm in width, and 21 μm in thickness (Fig. 2.5). We can also start from SOI wafers and skip the first two steps; however, it may further increase the cost due to the expensive unit price of SOI wafers. The fabrication process illustrates the application of Ti and Pt as the heating and sensing elements. The Ti/Pt sensing elements (strip of 280 μm in length by 2 μm in width) were encapsulated with Parylene C which was designed in direct contact with the blood flow.

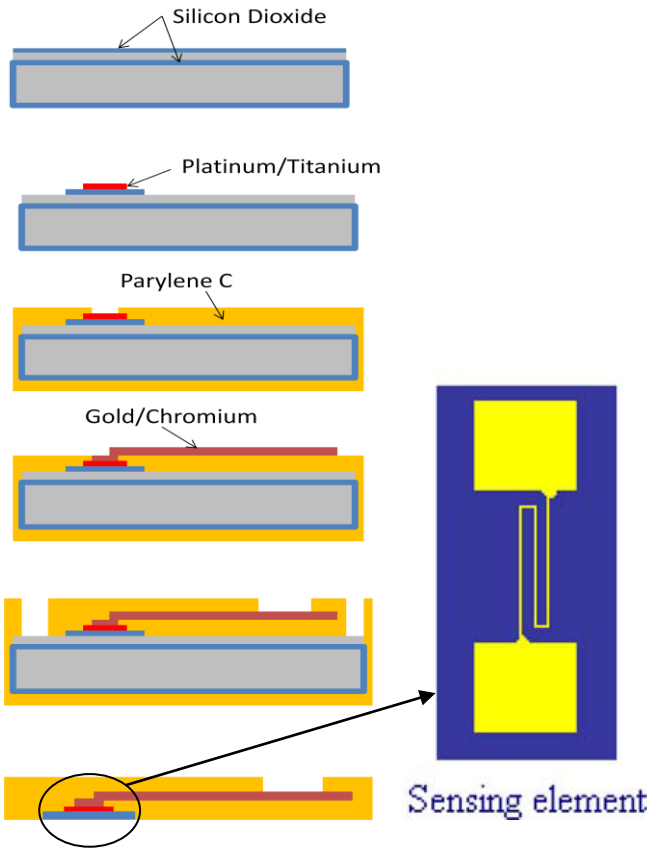

Figure 2.6 Fabrication process of the shear stress sensor. (a) Thermal growth of SiO_2 and deposition of sacrificial Si layer (1 μm). (b) Deposition and patterning of Ti/Pt layers (0.12 μm /0.02 μm) for the sensing element. (c) Deposition of Parylene C (9 μm). (d) Deposition and patterning of a metal layer of Cr/Au for electrode leads (0.6 μm). (e) Deposition and patterning of a thick layer of Parylene C (12 μm) to form the device structure. (f) Etching the underneath Si sacrificial layer leading to the final device.

2.3 Calibration

In order to obtain the relationship between shear stress and output voltage, we need to do the calibration. Based on the heat transfer principle, the output voltage of the MEMS sensors under the detection circuits was sensitive to the fluctuation in ambient temperature. The temperature overheat ratio (α_T) is defined as temperature variations of the sensor over the ambient temperature (T_0) (Schmidt et al. 1988)

$$\alpha_T = \frac{(T - T_0)}{T_0} \qquad \text{(Eq. 2.2)}$$

where T denotes the temperature of the sensor. The relation between resistance and temperature overheat ratios is expressed as

$$\alpha_R = \frac{(R - R_0)}{R} = \alpha(T - T_0) \qquad \text{(Eq. 2.3)}$$

where α is the TCR. For shear stress measurement, normally a high overheat ratio (~3 %) is used by passing higher current and by generating a “hot” sensing element to stabilize the sensor. Typically, a small pump system which can give flow rate is introduced to the calibration. We can directly obtain the relationship between output voltage and flow rate. However, due to different environment, the model connected wall shear stress and flow rate changes.

According to the application of the sensor, Yu (2008) proposed a method to calibration. 2-D (two-dimensional) flow channel was built for individual sensors to establish a relationship between heat exchange (from the heated sensing element to the flow field) and shear stress over a range of steady flow rates (Qn) in the presence of rabbit blood flow at 37.8 ˚C. For a Newtonian fluid at steady

state, the theoretical shear stress value in relation to the flow rate in the 2-D flow channel (Fig. 2.7) was established using the following formula based on the analysis of Truskey et al. (2004):

$$\tau_{xy}\big|_{y=\frac{H}{2},x=0} = \mu Q \cdot \frac{6 - \sum_{n=0}^{\infty} \frac{48}{(2n+1)^2 \pi^2 \cosh\left(\frac{(2n+1)\pi W}{2H}\right)}}{WH^2 - \sum_{n=0}^{\infty} \frac{96H^3}{(2n+1)^5 \pi^5 \cosh\left(\frac{(2n+1)\pi W}{2H}\right)} \cdot \exp\left(\frac{(2n+1)\pi W}{2H}\right)} \qquad \text{(Eq. 2.4)}$$

$$y \in \left(-\frac{H}{2}, \frac{H}{2}\right), \quad x \in \left(-\frac{W}{2}, \frac{W}{2}\right)$$

where τ is the wall shear stress, μ is the blood viscosity, and H and W are the height and the width of the flow channel, respectively (H/W = 0.433). The viscosity used in the aforementioned equation was obtained from the published data for rabbit blood (Longest et al. 2003).

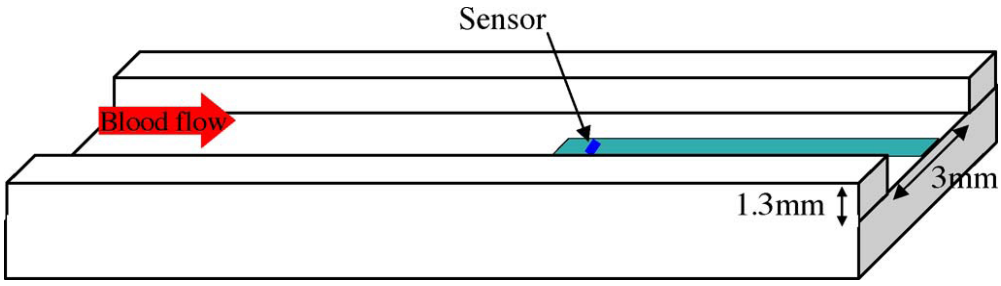

Figure 2.7 Schematic diagram of 2-D micro PDMS channel for sensor calibration in the rabbit blood. The sensor body was flush-mounted on the floor of the channel at a sufficient entrance length to allow for fully developed laminar flow before reaching the sensor (Yu et al. 2008).

2.4 Circuitry

There are two types of control and readout modes: constant-current (CC) (Fig. 2.8) and constant-temperature (CT) (Fig. 2.9) modes. As shown in Fig. 2.8, CC circuit is very simple. R_s is the resistance of the sensing element of thermal flow sensor. The DC bias voltage and R set both the positive and negative inputs of the amplifier. Due to the high input impedance of the amplifier, the current

flow through R and R_s are the same. Adjusting the R_s/R to a certain value, we can set the current I constant. Terminal E_t is used for frequency response testing.

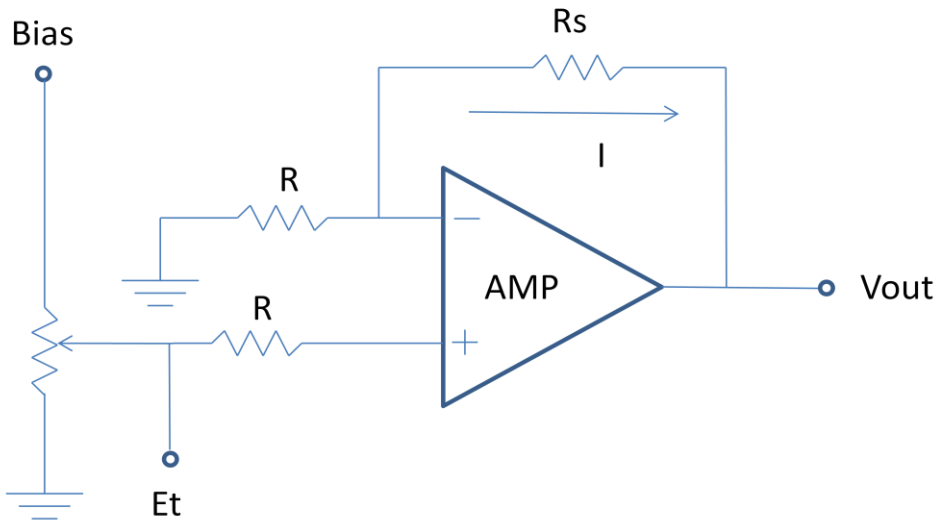

Figure 2.8 A constant-current circuit for thermal flow sensor

As mentioned in Chapter 1, the relation between temperature and sensing element is linear (Eq. 1.6). Any increase of flow velocity from the surrounding fluid will cause the sensor R to cool down. Because of the temperature coefficient of resistance α, this cooling will cause a decrease in R. R is in the Wheatstone bridge with R_1, R_2 and R_3, any change in R will change the voltage distribution, in this case, an increase in voltage difference between positive and negative input of the amplifier, thus an increase in amplifier output E_{out}. Meanwihle the negative feedback from the output of the amplifier to the top of the resistor bridge acts to largely bring down the voltage across each resistance, in other words, maintaining the resistance of the sensor and hence, keeps the average temperature essentially constant. Fig. 2.9 is the typical CT circuit, a Wheatstone bridge and a differential operational amplifier as previously reported. Initially, the switch was set to

determine the cold resistance of the sensor. The resistor was then adjusted to establish a slightly higher operating resistance by R_{oh}. The voltage signals in responses to variations in heat transfer were detected via E_t.

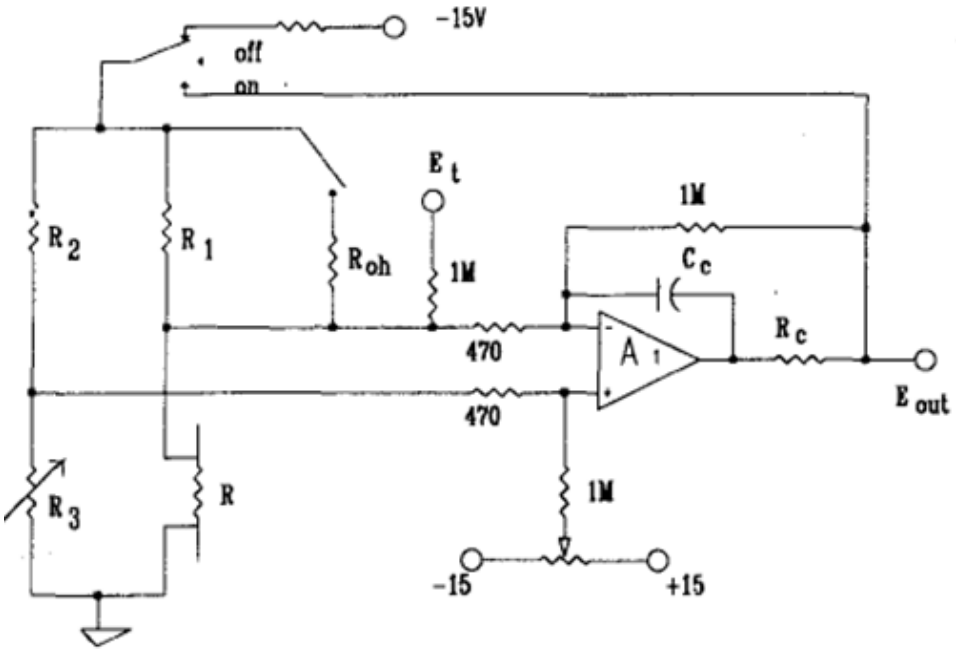

Figure 2.9 Schematic of constant-temperature mode (CT) circuit diagram to drive the MEMS sensor. The Wheatstone bridge network was coupled with an operational amplifier as a feedback circuit. (Huang et al. 1995)

Normally, CT mode has a higher sensitivity than that of the CC mode (Fig. 1.6), especially in large shear stress range, because the CC mode shows saturation with the increasing of shear stress, shown in Fig. 2.10.

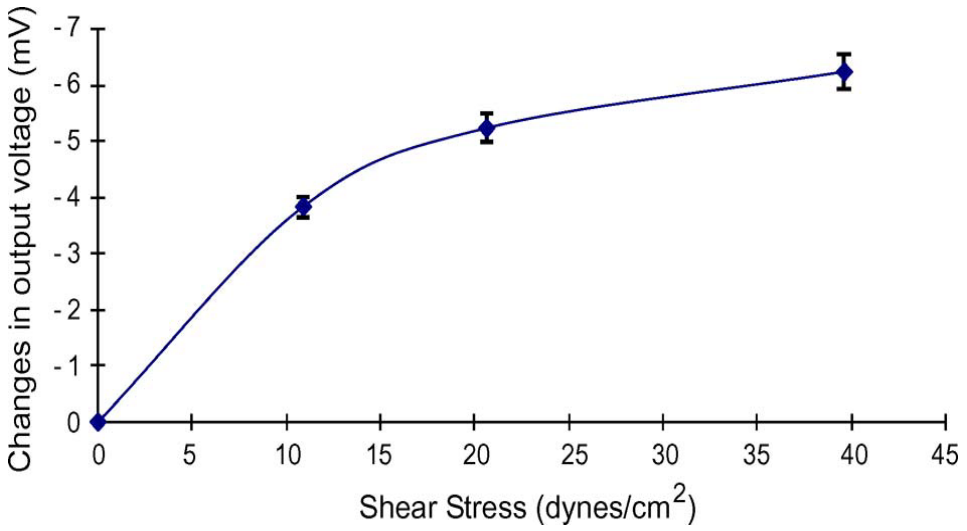

Figure 2.10 Output voltage response with shear stress change, the output voltage saturated in large shear stress region (Yu et al. 2008).

We designed a CT circuit for our thermal flow sensor (Fig. 2.11). Our sensor was designed to be an anemometer, which meant that the mechanism used to measure the flow speed involves heating a resistor (the anemometer) by passing current through it and measuring the amount heat removed from the resistor that was delivered to the flowing fluid (water). This sensor worked under the assumption that the primary mechanism of heat transfer between the resistor and the fluid was through convection and that conduction and radiation contribute negligible heat transfer from the heated resistor. To ensure this assumption, we operated the resistor at a temperature ~10 ˚C above the expected ambient temperature of the fluid to minimize radiative effects which scale as ΔT^4. We also fabricated the device so that a thermal insulator was underneath the metal resistor to minimize conductive heat transfer to the substrate.

In this session, we emphasized on an amplifier which had relatively large output swing (approximately 1V) and large DC gain (about 69dB). The feedback

will adjust the Wheatstone bridge voltage U_B by applying a ΔU (Fig. 2.11 (a)). The larger output swing the amplifier can give, the larger ΔU will be, and thus the larger ΔI will flow through Wheatstone bridge. ΔI will affect the heat generated by sensing element and bring the bridge back to equilibrium. Based on the above mechanism, we think large output swing can improve the thermal response of the system.

Table 2.1 Size of all the transistors

Transistor	Width	Length
M1	60 μm	600 nm
M2	60 μm	600 nm
M3	32 μm	2.4 μm
M4	90 μm	600 nm
M5	90 μm	600 nm
M6	90 μm	600 nm
M7	90 μm	600 nm
M8	36 μm	600 nm
M9	36 μm	600 nm
M10	36 μm	600 nm
M11	36 μm	600 nm

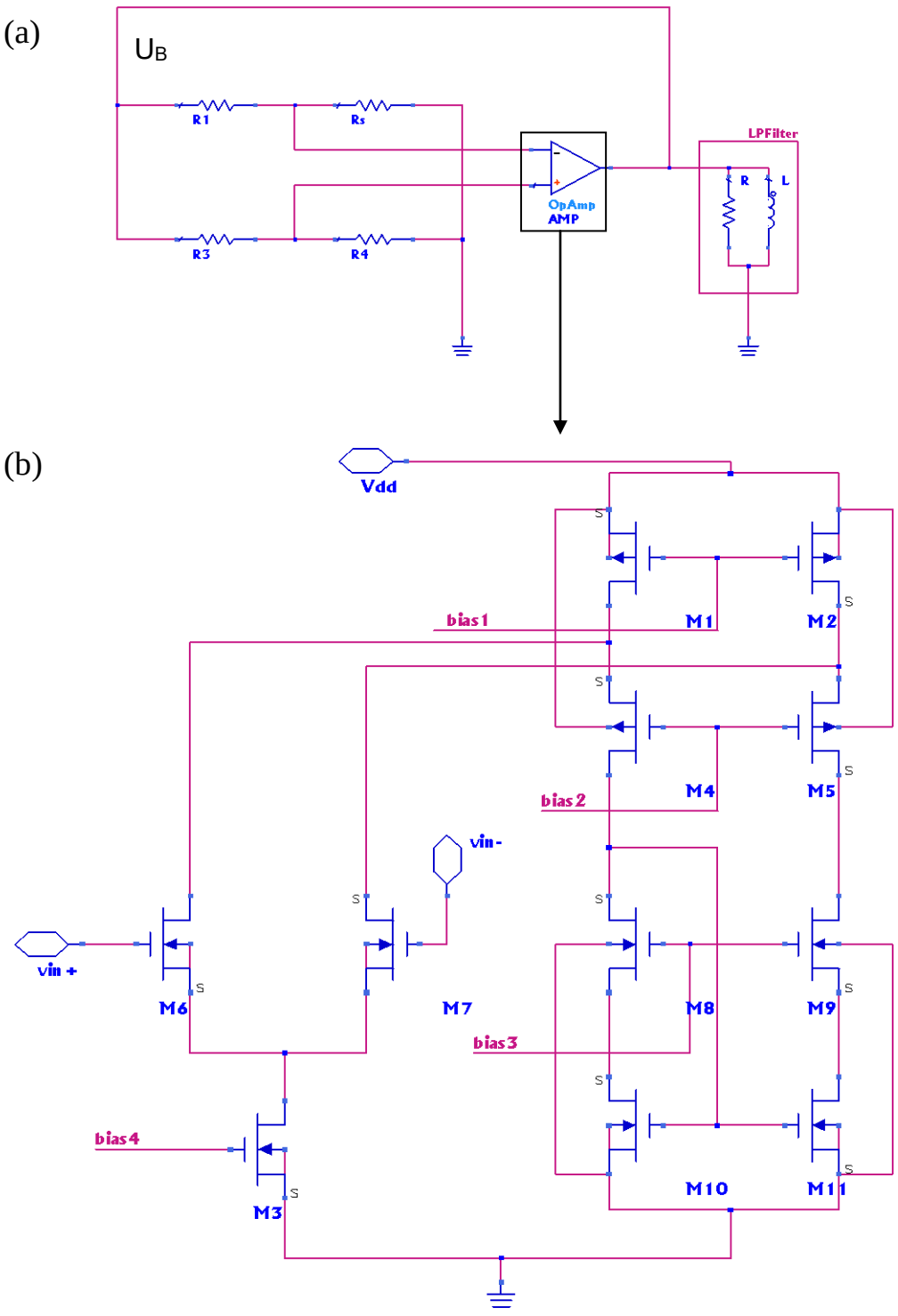

Figure 2.11 Schematic of designed circuits (a) read-out system (b) schematic of designed amplifier

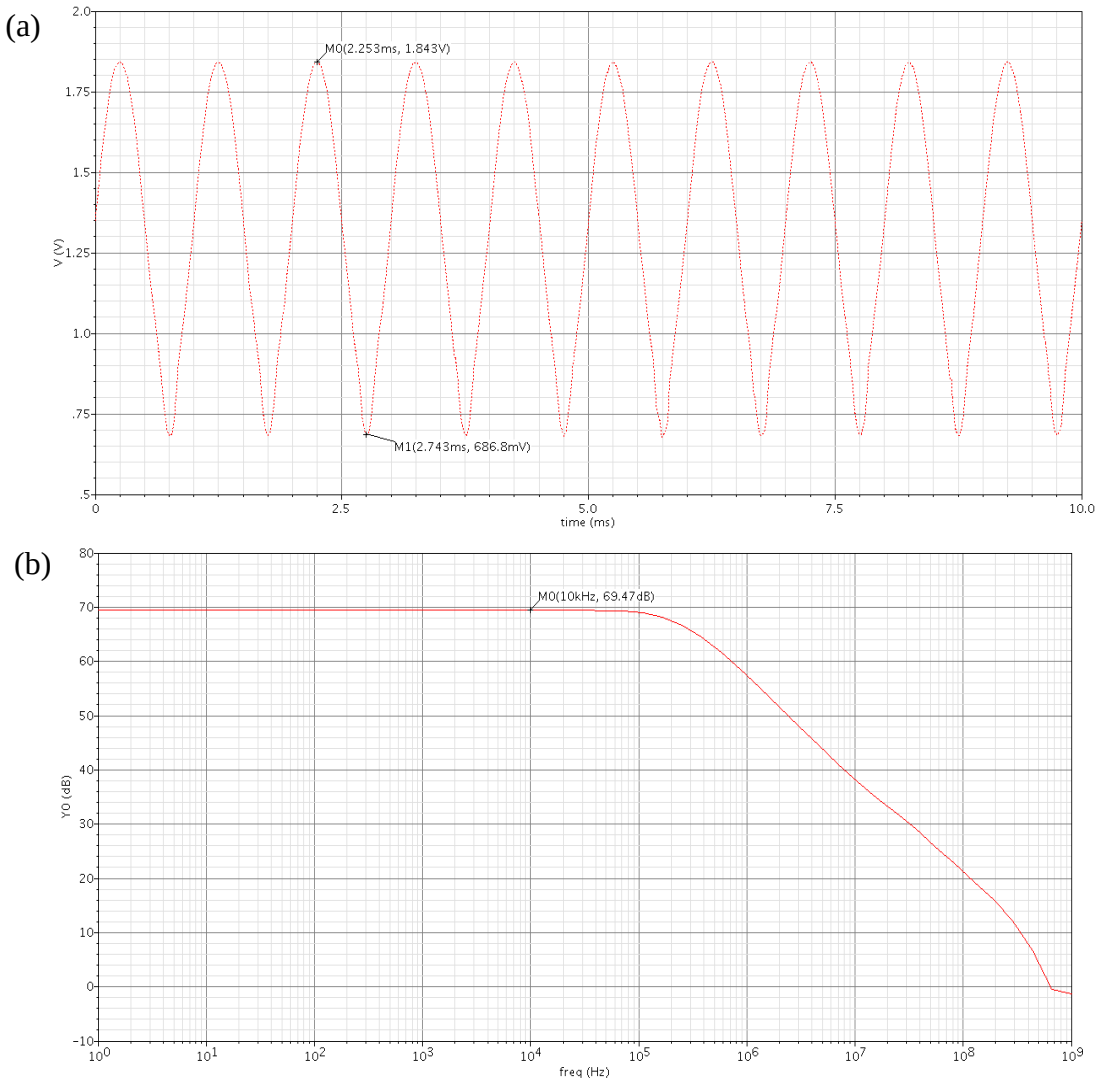

Figure 2.12 Simulation results (a) Maximum output voltage swing about 1 V (b) DC voltage gain about 69dB

For the amplifier, it was designed using AMI C5N library (0.6 μm process) and all the transistor size listed in Table 2.1. Simulation results are shown in Fig. 2.12. Currently, the author was focusing on further testing the circuit through simulation software Cadence and designing layout. Another important thing was that this large output swing differential amplifier was used to drive a resistive load instead of small capacitive load, so an output buffer stage was necessary otherwise the gain would drop dramatically due to the effect of the resistive load. In addition, the thermal flow sensor was working at

very low frequency (lower than 10 kHz). A low pass filter at the output side needed to be designed in future work.

Chapter 3

THREE DIMENSIONAL THERMAL FLOW SENSORS

In Chapter 2, a flexible thermal flow sensor for intravascular shear stress analysis was introduced. However, according to its structures, each flexible sensor has only one single sensing element (1-D data collector). For the intravascular shear stress analysis application, when the sensor was inserted into blood vessels (specifically aorta), it was impossible to make the sensor exactly to the wall of the vessels; on the other hand, the equation between shear stress and flow rate (Eq. 2.4) was generated from a PDMS (Polydimethylsiloxane) channel which shear stress sensors mounted on its floor. Obviously, the shear stress was different from place to place in a blood vessel; in addition, the sensor itself would also change the shear stress distribution as well. Thus, if we only have 1-D sensor to obtain data, we can hardly figure out what really happened inside blood vessels. Based on above problems of current technology, a 3-D structure was proposed with three sensing elements in three independent axes in each sensor. This will definitely give us more data. And based on these data, it will give us a better understanding of shear stress distribution in the presence of time-varying component of blood flow and it is also possible for us to build more accurate computational fluid dynamics (CFD) model and realize more accurate assessment of intravascular shear stress as well as convective heat transfer through simulation.

3.1 Design and fabrication of 3-D thermal flow sensors

The previous 1-D shear stress sensor was based on flexible polymer Parylene C and biocompatible sensing element Ti/Pt. Based on this technology, the 3-D thermal flow sensor was designed similarly as a hexagonal prism consisted of silicon substrate and

external wires (Fig. 3.1). On the top of silicon substrate, there were four bond pads for external wires sandwiched by Parylene.

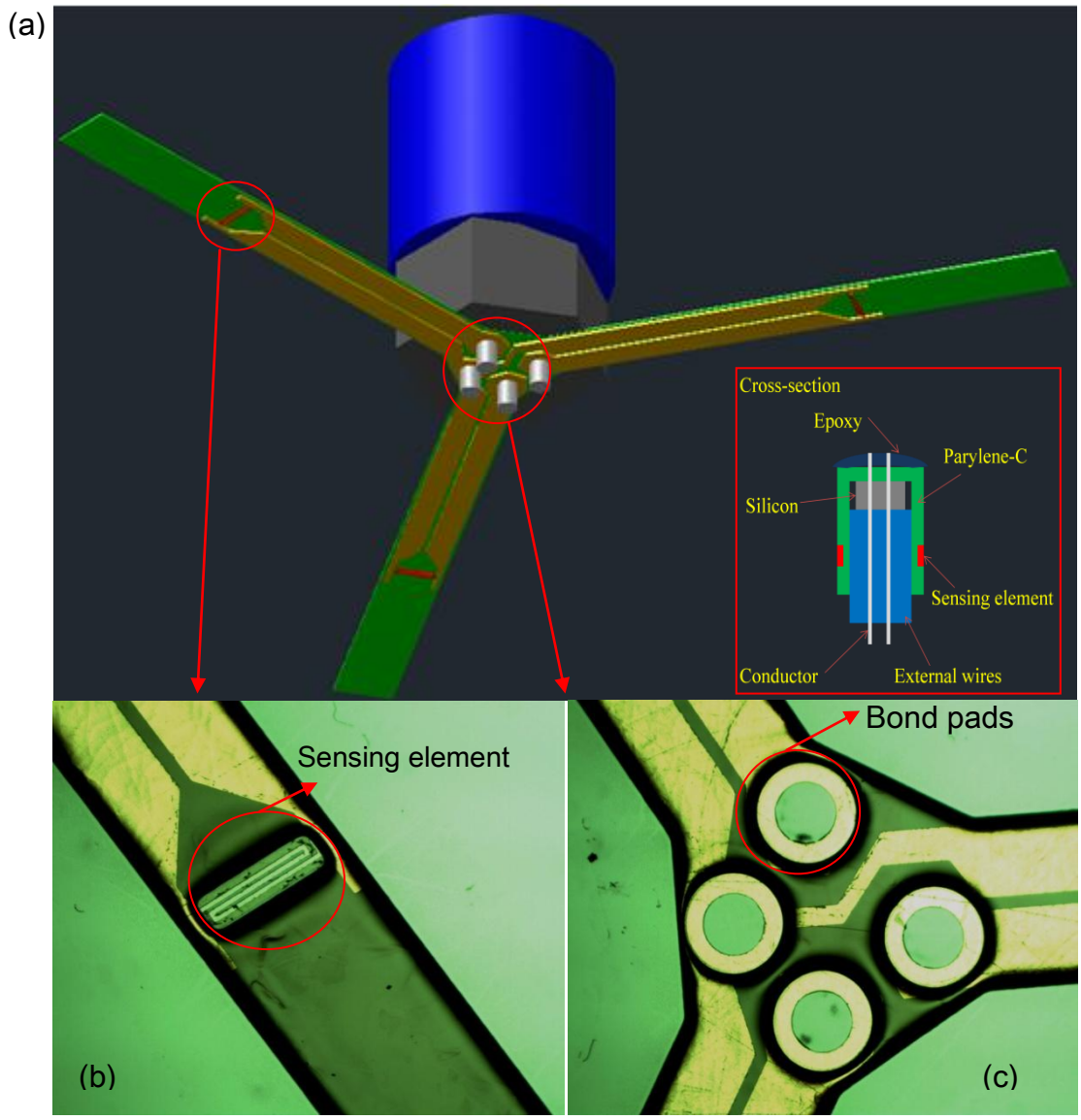

Figure 3.1 Schematic of 3-D thermal flow sensor (a) 3-D view of the flow sensor (b) sensing element was strip 1400 μm in length and 10 μm in width (c) Bond pads were 200 μm in diameter.

In each nonadjacent side surface of silicon substrate, there was a sensing element supported by bent Parylene layer. Fig. 3.1 shows the schematic of 3-D thermal flow sensor.

The sensor bodies consisted of 3 independent Parylene bridges; each was 5 cm in length, 580 μm in width, and approximately 21 μm in thickness (Fig. 3.1(a)). And these bridges will be bent and attach to the silicon substrate and external wires through epoxy. The Ti/Pt sensing elements located in each bridge are nothing but strips 1400 μm in length by 10 μm in width, shown in Fig. 3.1(b). The bond pads which are used to connect external wires are 200 μm in diameter, shown in Fig. 3.1(c).

The sensing element was fabricated using surface micromachining with biocompatible materials including Ti, Pt and Parylene C. The fabrication process is as the following: 1) start with a bare silicon wafer, deposit a Parylene C thin layer 10 μm (with A-174 adhesion promoter); 2) deposit and pattern a 0.1μm silicon dioxide with e-beam evaporator to form a blocker to prevent RIE etching through Parylene in the following steps, 20nm Cr was used to enhance the adhesion between silicon dioxide and Parylene; 3) deposit Ti/Pt layers with thickness of 0.12 μm/0.02 μm for the sensing element with e-beam evaporator, and pattern these layers using lift-off (AZ5214 photoresist) to form a 10 μm metal traces, after that, deposit Cr/Au 0.02 μm /0.6 μm for interconnection with e-beam evaporator; 4) deposition of 10 μm Parylene C with Parylene vacuum coating system and pattern Parylene C layer using photolithography and oxygen plasma. Because the etching rate between Parylene C and photoresist is very close, approximately 7:8, the Parylene C is etched even faster; more than 20 μm thick photoresist is needed accordingly; 5) spin and pattern photoresist on the backside of the silicon wafer, then hard bake for 30 minutes; 6) use DRIE (Deep reactive-ion etching) to etch silicon from backside to release the sensor structure leading to the final device, shown in Fig 3.2.

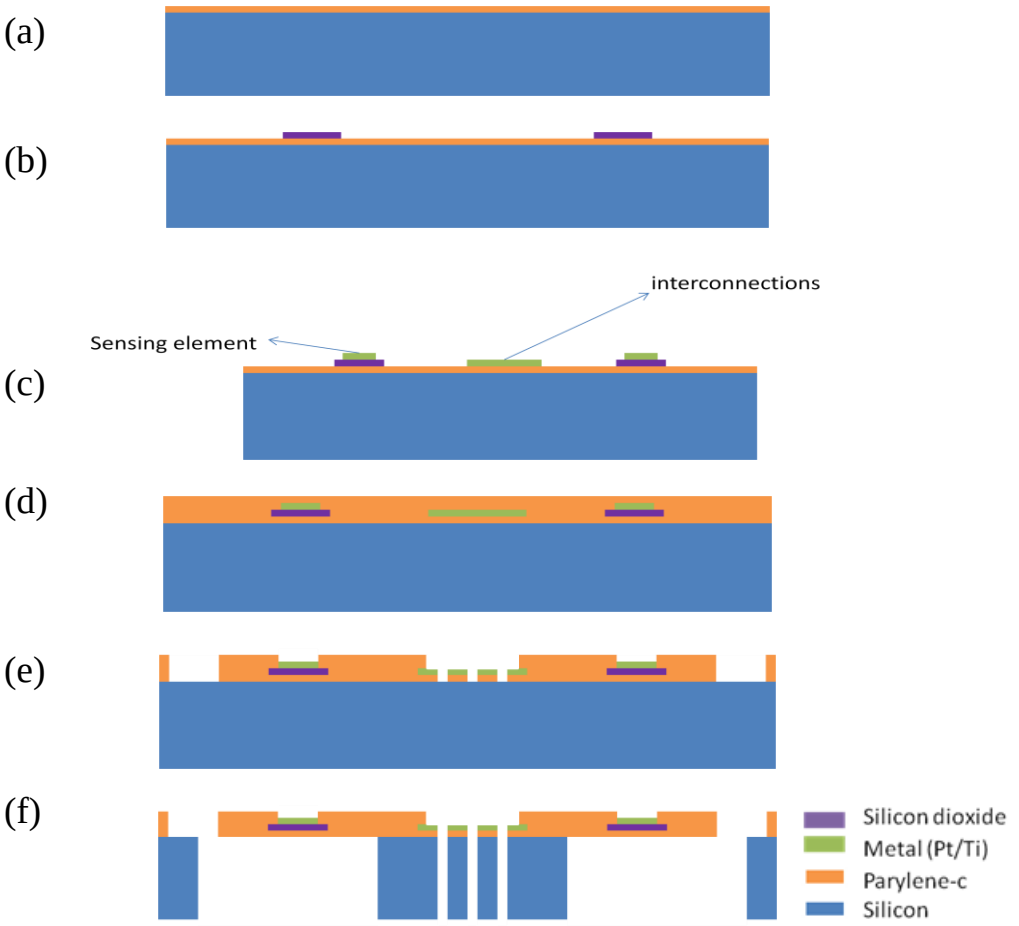

Figure 3.2 Fabrication of the sensor (a) deposition of Parylene (b) deposition and pattern of silicon dioxide (c) deposition and pattern of sensing element and interconnection (d) deposition of another layer of Parylene (e) pattern Parylene (f) backside DRIE etching and sensor releasing.

3.2 Problems analysis in fabrication process

The first problem happened during the fabrication process was the adhesion between Parylene and silicon substrate. Because there were three lift-off processes, soaking in acetone for a long time would cause slight peeling of the Parylene. In order to solve this problem, A-174 adhesion promoter was used before thermal evaporation of Parylene.

The second problem was that during the process, 0.6 μm thick gold needed to be deposited (in order to reduce the noise generated by interconnection, we wanted to make the resistance of interconnection as small as possible), the heat generated from the deposition was too large for photoresist, even the vaccum went down to 10^{-7} mTorr. The heat would bake the photoresist and make the lift-off extremely hard. The solution is rather than depositing the gold in one time, depositing 0.2 μm gold then vent the chamber and let the nitrogen come out and hold for 10 minutes to cool down everything, then repeat the above process another two times until we get 0.6 μm thick gold. This method is time consuming due to long pump down time. Another solution for this problem is wet etching rather than lift-off.

The third problem was in Parylene etching. After the Parylene etching, a thin layer photoresist should be removed in acetone. But the RIE (Reactive-ion etching) made photoresist very hard to be removed completely (Fig. 3.3), we soaked it in acetone for more than 1 hour, and tried heat it up around 80 ˚C. However, still could not remove photoresist completely. Then if soak the sample in ultrasonic for about 20-30 seconds, the Parylene starts to peel off as well as photoresist. This is probably because the contamination inside chamber changes the characteristic of photoresist. To get rid of contamination, dummy run is essential.

The most critical step was backside etching which is the final step. Because of the unique structure of the sensor, the silicon substrate was etched all the way through. As the etching went deeper and deeper, the silicon substrate became thinner and thinner. Gradually, the pressure generated from cooling gas would exceed the tolerance of the wafer, breaking the wafer at a certain point (Fig. 3.4). The normal way to reduce the risk

of breaking wafers is using a dummy wafer attached to the sample. In our experiment, the dummy wafer worked as a thermal insulator that largely reduced the heat conduction from the cooling system. The heat baked the photoresist as well as the Parylene. Fig 3.5 is the Parylene after several hundred cycles of DRIE. The Parylene pattern is full of cracks which mean it is seriously baked and lose its flexibility.

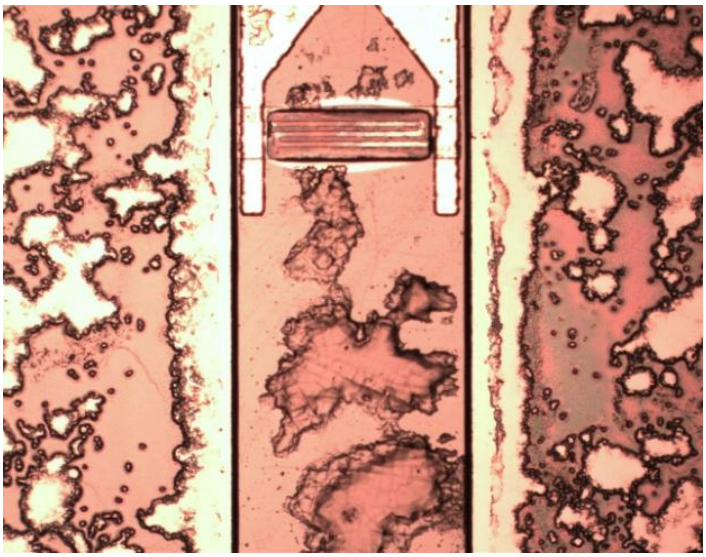

Figure 3.3 Photoresist residues on top of Parylene after RIE etching

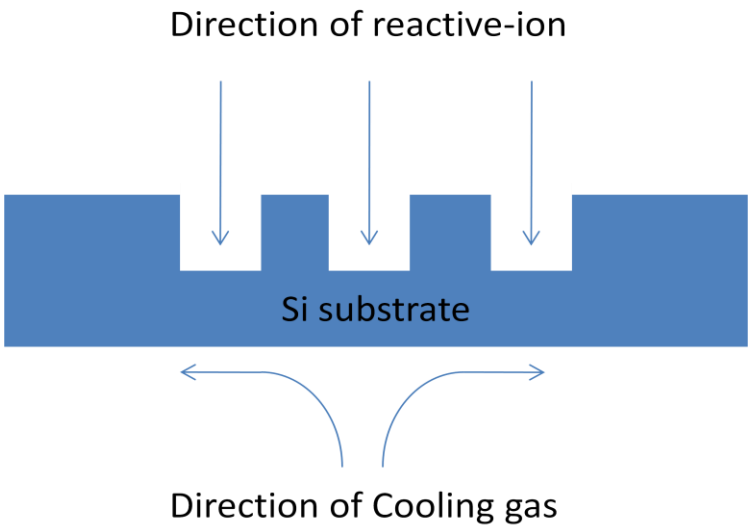

Figure 3.4 Demonstration of various pressures during DRIE

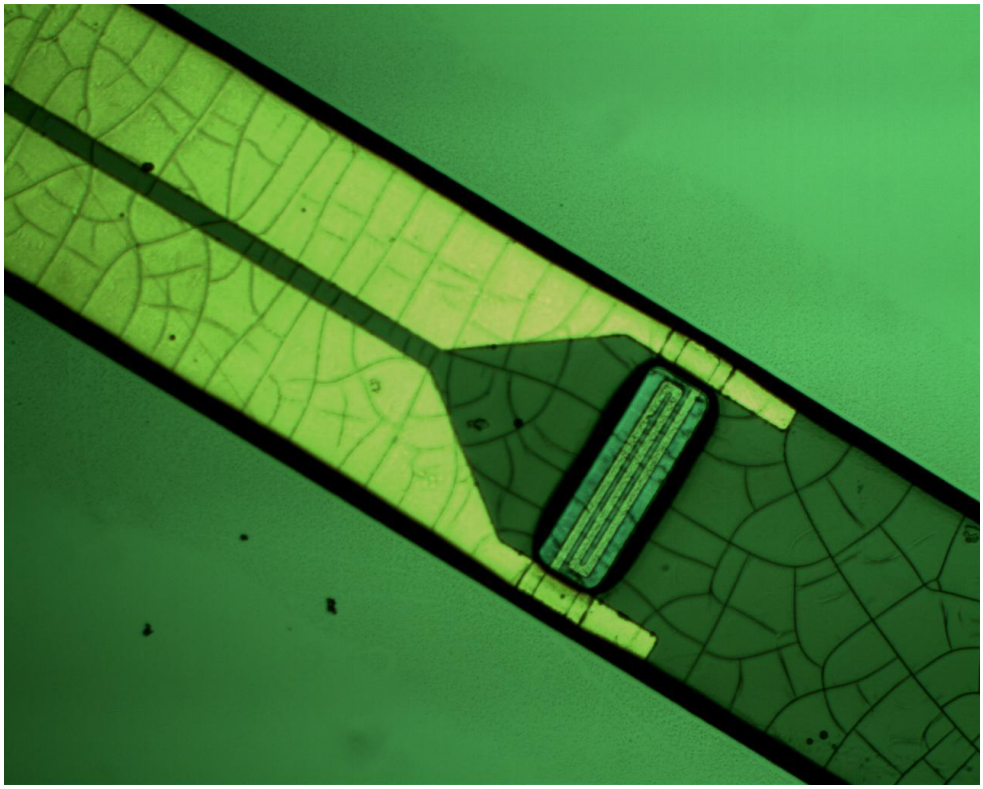

Figure 3.5 The view of Parylene cracks after DRIE

3.3 Computational fluid dynamics (CFD)

Previously discussed in the beginning of Chapter 3, the 3-D thermal flow sensor has three sensing element located in different axes to obtain data. Even in this way, it is hard to know the intravascular shear stress distribution due to the sensor location varying each time. In order to realize more accurate assessment of intravascular shear stress as well as convective heat transfer, simulation, specifically CFD model, is of great importance for this intravascular monitoring.

Ai et al. from USC (University of Southern California) biomedical group developed three dimensional CFD code for non-Newtonian fluid to simulate shear stress in the eccentric stenotic model. According to their *in-vivo* test, the average diameter of the rabbit abdominal aortas, Dave = 2.4 mm, was measured during catheterization. The non-

Newtonian blood flow was simulated using the 3-D Navier–Stokes equations. The governing equations, including mass and momentum equations, were solved in FLUENT software for laminar, incompressible, and non-Newtonian flow. Briefly, the CFD model was constructed with 2, 410, 112 cells, which were primarily the tetrahedral elements. Fine elements, especially immediately adjacent to the tube wall and in the vicinity of the stenosis, were constructed to obtain sufficient information to characterize the large fluid velocity gradients near the wall. This approach guaranteed the mesh-independence of the numerical results. The simulations were performed under three steady state flow rates, namely, 50, 100, and 150 mL/min. The simulation results were shown in Fig. 3.6.

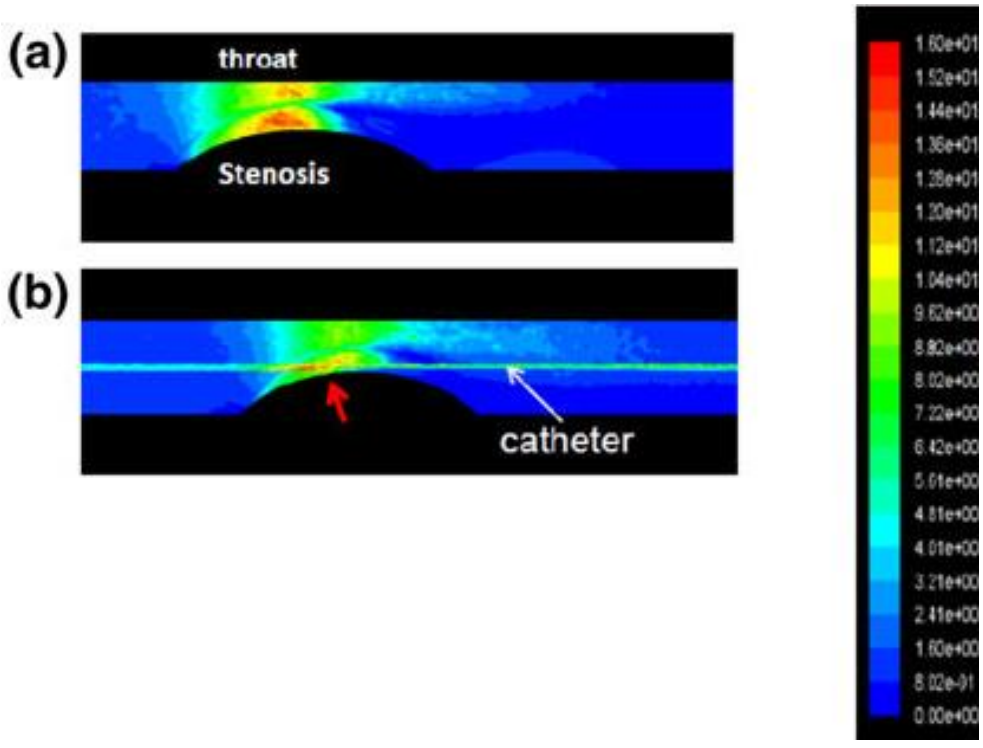

Figure 3.6 A representative CFD simulation for the 3-D eccentric stenotic model at a steady flow rate of 150 mL/min. (a) The wall shear stress profiles reveal the highest magnitude alone the throat corresponding to the region of highest mean velocity, and lowest magnitude in the zone of flow reversal. (b) Intravascular shear stress (ISS) on the catheter along the axial position peaks in the throat, and reached a nadir in the zone of flow reversal. (Yu et al. 2011)

Chapter 4

CONCLUSIONS AND FUTURE WORK

4.1 Conclusions

This thesis explored two types of thermal flow sensors for intravascular shear stress analysis. Both of them were based on heat transfer principle, heat convection from the resistively heated element to the flowing fluid is measured as a function of the changes in voltage, from which wall shear stress can be inferred. For both sensors, the resistively heated element sharing the same design worked as a heater in the same time as a sensing element. It was made of Ti/Pt strip with the thickness 0.12 μm and 0.02 μm. The resistance of the sensing element was measured at approximately 1.6-1.7 kΩ. A linear relation was established over the temperature ranging from 22 ˚C to 80 ˚C and the TCR was at approximately 0.12 %/˚C.

The structures of these sensors were different, the first thermal flow sensor was 1-D shear stress sensor, which had one axis of sensing element, utilizing Parylene C to provide both insulation of electrodes and flexibility of the sensors. The size of sensing element was 280 μm in length and 2 μm in width strip. The total sensor bodies were 4 cm in length, 320 μm in width, and 21 μm in thickness, using surface micromachining. For shear stress measurement, normally a high overheat ratio (~3 %) is used by passing higher current and by generating a "hot" sensing element to stabilize the sensor. In order to obtain electrical signals, especially voltage changes in this case, a constant-temperature circuit was designed based on AMI C5N library (0.6 μm process).

Although 1-D flexible shear stress sensor was promising for arterial system analysis, there was one important problem. When the sensor was inserted into blood vessels

(specifically aorta), it was impossible to locate the sensor exactly to the wall of the vessels. From the previous simulation work of Ai et al. (2009), the shear stress was varying and the sensor itself changed the distribution as well. Due to this problem, the measurement error could be great. We proposed a 3-D thermal flow sensor, which three axis of sensing element integrated in one sensor. Thus, with CFD simulation, it is possible to locate the sensors in blood vessels. On the other hand, more data from sensors will help us optimize the CFD model.

The 3-D thermal flow sensor was designed in the shape of hexagonal prism with diagonal 1000 μm. In each nonadjacent side surface, there was a sensing element with the size of strip 1400 μm in length and 10 μm in width. On the top, there were five bond pads for external wires sandwiched by Parylene over 500 μm thick silicon substrate. This kind of bended structure was realized by surface micromachining and DRIE release. The 3-D thermal flow sensor was under fabrication due to the problem happened in the final step which was backside DRIE. During the DRIE process, the large heat generated from physical bombardment baked the Parylene, causing a lot of cracks.

4.2 Future work

As discussed in previous chapters, the CT circuit had a relatively better resolution compared with CC circuit. In our project, we designed a CT circuit as a read-out circuit for the thermal sensors. However, our current design of amplifier is a differential amplifier. Normally, the differential amplifier is used to drive a small capacitive load instead of a resistive load. However, in this design, the amplifier was used to drive a Wheatstone bridge, so an output buffer stage is necessary otherwise the gain will drop

dramatically. In addition, the thermal flow sensor is working at very low frequency. A low pass filter needs to be designed in the future to reduce noise level.

For the 3-D thermal flow sensor, device fabrication is only starting point of the project. After that, packaging, calibration, *in-vivo* testing and CFD modeling will be further investigated in the future. How to package the released sensor and make it bended without breaking the metal interconnection is a challenge issue which needs to be emphasized. Brief calibration settings were shown in Fig. 4.1.

In conclusion, the 3-D thermal sensor based on its special structures not only has a possibility to solve problems exiting in 1-D shear stress sensors and also gives us a unique package method for sensing applications.

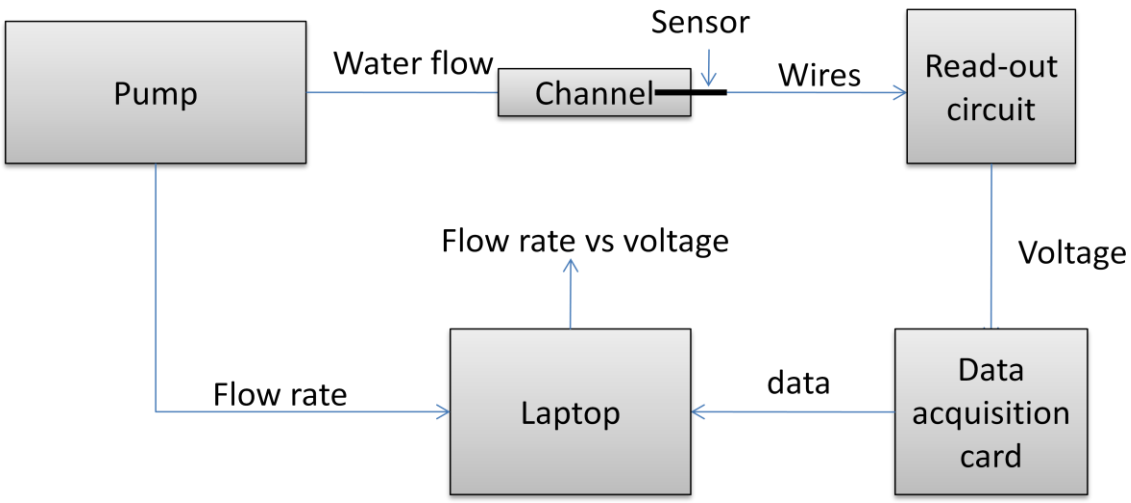

Figure 4.1 Flow of calibration set up for 3-D thermal flow sensor

REFERENCES

Ai, L. S., H. Y. Yu, W. Dai, S. L. Hale, R. A. Kloner, T. K. Hsiai. 2009. Real-time intravascular shear stress in the rabbit abdominal aorta. *IEEE Transactions on Biomedical Engineering* 56(6):1755–1764.

Ai, L. S., H. Y. Yu, W. Takabe, A. Paraboschi, F. Yu, E. S. Kim, R. Li, T. K. Hsiai. 2009. Optimization of intravascular shear stress assessment *in vivo*. *Journal of Biomechanics* 42(10):1429–1437.

Ashauer, M., H. Glosch, F. Hedrich, N. Hey, H. Sandmaier, W. Lang. 1998. Thermal flow sensor for liquids and gases, *Proceedings of Micro Electro Mechanical Systems*.

Berger, S. A., L. D. Jou. 2000. Flows in stenotic vessels. *Annual Review of Fluid Mechanics* 32:347–382.

Cain, A., T. Nishida, and M. Sheplak. 2000. Development of a wafer-bonded, silicon-nitride membrane thermal shear-stress sensor with platinum sensing element. *In Proceeding of Solid-State Sensors and Actuators Workshop*.

Davies, P. F., C. F. Dewey, Jr., S. R. Bussolari, E. J. Gordon, M. A. Gimbrone, Jr. 1984. Influence of hemodynamic forces on vascular endothelial function. In vitro studies of shear stress and pinocytosis in bovine aortic cells. *Journal of Clinical Investigation* 73(4):1121–1129.

Fan, Z., J. M. Engel, J. Chen, C. Liu. 2004. Parylene surface-micromachined membranes for sensor applications. IEEE *Journal of Microelectromechanical Systems* 13(3): 484–490.

Frauenfelder, T., E. Boutsianis, T. Schertler, L. Husmann, S. Leschka, D. Poulikakos, B. Marincek, H. Alkadhi. 2007. Flow and wall shear stress in end-to-side and side-to-side anastomosis of venous coronary artery bypass grafts. *BioMedical Engineering OnLine* 6: 35.

Fung, Y. C. 1997. *Biomechanics: Circulation, second edition*. New York: Springer-Verlag.

Gupta, B., R. Goodman, F. Jiang, Y. C. Tai. 1996. Analog VLSI system for active drag reduction. *IEEE Journal of Microelectromechanical Systems* 16(5): 53–59.

Haritonidis, J. H. 1989. *Advances in Fluid Mechanics Measurements*, Berlin: Springer.

Ho, C. M., Y. C. Tai, 1998, Micro-electro-mechanical-systems and fluid flows. *Annual Review of Fluid Mechanics* 30: 579–612.

Hsiai, T. K., S. K. Cho, P. K. Wang, M. H. Ing, A. Salazar, S. Hama, M. Navab, L. L. Demer, C. M. Ho. 2004. Micro sensors: linking vascular inflammatory responses with real-time oscillatory shear stress. *Annals of Biomedical Engineering* 32(2): 189–201.

Huang, J. B., F. K. Jiang, Y. C. Tai, C. M. Ho. 1999. A micro-electro-mechanical system-based thermal shear-stress sensor with self-frequency compensation. *Measurement Science and Technology* 10(8): 687–696.

Ku, D. D. 1997. Blood flow in arteries. *Annual Review of Fluid Mechanics* 29: 399–434.

Lofdahl, L., G. Stemme, B. Johansson. 1989. A sensor based on silicon technology for turbulence measurements. *Journal of Physics E: Scientific Instruments* 22: 391–393.

Longest, P. W., C. Kleinstreuer, G. A. Truskey, J. R. Buchanan. 2003. Relation between near-wall residence times of monocytes and early lesion growth in the rabbit aorto-celiac junction. *Annals of Biomedical Engineering* 31(1): 53–64.

Melani, M., L. Bertini, M. De Marinis, P. Lange, F. D. Ascoli, L. Fanucci. 2008. Hot wire anemometric MEMS sensor for water flow monitoring. *Design, Automation and Test in Europe* 342–347.

Meng, E., Y. C. Tai. 2003. A Parylene MEMS flow sensing array, *Proceeding of the 16th International Conference on Solid-State Sensors, Actuators and Microsystems* 686–689.

Nerem, R. M., R. W. Alexander, D. C. Chappell, R. M. Medford, S. E. Varner, W. R. Taylor. 1998. The study of the influence of flow on vascular endothelial biology. *The American Journal of the Medical Sciences* 316(3): 169–175.

Rasmussen, A., M. E. Zaghloul. 1998. In the flow with MEMS. *Circuits and Devices Magazine* 14(4): 12-25.

Rouhanizadeh, M., G. Soundararajan, R. Lo, D. Arcas, F. Browand, T. Hsiai. 2006. MEMS sensors to resolve spatial variations in shear stress in a 3-D blood vessel bifurcation model. *IEEE Sensors Journal* 6(1): 78-88.

Schmidt, M. A., R. T. Howe, S. D. Senturia, J. H. Haritonidis. 1988. Design and calibration of a microfabricated floating-element shear-stress sensor. *IEEE Transactions on Electron Devices* 35(6): 750–757.

Soulis, J. V., G. D. Giannoglou, Y. S. Chatzizisis, T. M. Farmakis, G. A. Giannakoulas, G. E. Parcharidis, G. E. Louridas. 2006. Spatial and phasic oscillation of non-Newtonian wall shear stress in human left coronary artery bifurcation: An insight to atherogenesis. *Coronary Artery Disease* 17(4): 351–358.

Soundararajan, G., M. Rouhanizadeh, H. Yu, E. S. Kim, T. K. Hsiai. 2005. MEMS shear stress sensors for microcirculation. *Sensors and Actuators: A* 118(1): 25–32.

Stemme, G. 1988. A CMOS integrated silicon gas-flow sensor with pulse-modulated output. *Sensors and Actuators* 14(3): 293–303.

Tabata, O., H. Inagaki, I. Igarashi, T. Kitano. 1985. Fast response silicon flow sensor with a thermal isolation structure. *Proceeding of the 5th Sensor Symposium* 207–211.

Taylor, C. A., T. J. T. Hughes, C. K. Zarins. 1998. Finite element modeling of three-dimensional pulsatile flow in the abdominal aorta: Relevanceto atherosclerosis. *Annals of Biomedical Engineering* 26(6): 975–987.

Topper, J. N., J. Cai, D. Falb, M. A. Gimbrone, Jr. 1996. Identification of vascular endothelial genes differentially responsive to fluid mechanical stimuli: Cyclooxygenase-2,

manganese superoxide dismutase, and endothelial cell nitric oxide synthase are selectively up-regulated by steady laminar shear stress. *Proceedings of the National Academy of Sciences* 93(19): 10417–10422.

Truskey, G., F. Yuan, D. Katz. 2004. *Transport Phenomena in Biological Systems*. New Jersey: Pearson Prentice Hall.

Van Oudheusden, B. W. 1988. Silicon flow sensors. *Control Theory and Applications, IEE Proceedings D* 135(5): 373-380.

Van Putten, A. F. P. 1983. An integrated silicon double bridge anemometer. *Sensors and Actuators* 4: 387–396.

Womersley, J. R. 1955. Method for the calculation of velocity, rate of flow and viscous drag in arteries when the pressure gradient is known. *The Journal of Physiology* 127(3): 553–563.

Yu, F., L. S. Ai, W. D. Dai, N. Rozengurt, H. Y. Yu, T. K. Hsiai. 2011. MEMS thermal sensors to detect changes in heat transfer in the pre-atherosclerotic regions of fat-fed New Zealand white rabbits. *Annals of Biomedical Engineering* 39(6): 1736-1744.

Yu, H., L. S. Ai, M. Rouhanizadeh, D. Patel, E. S. Kim, T. K. Hsiai. 2008. Flexible polymer sensors for *in vivo* intravascular shear stress analysis. *IEEE Journal of Microelectromechanical Systems* 17(5): 1178–1186.